A Robust Switched Filter Design for Grid-to-Vehicle Battery Charging Scheme Using Whale Optimization Algorithm

Ahmed I. Omar[1*]

ABSTRACT

Abstract— This paper introduces a novel grid-to-vehicle (G2V) battery charging scheme that utilizes a Li-ion battery-supercapacitor storage system as a backup AC/DC interface to ensure a robust, decoupled interface, power factor enhancement, and power quality performance of an AC grid utility system. A distributed FACTS-based switched filter compensator (SFC) structure is employed as the primary goal to ensure the energy-efficient utilization of the vehicle-to-home (V2H) battery charging scheme under various operational modes. An optimal multi-level functional error-driven weighted modelled proportional-integral-derivative (WM-PID) control strategy was employed to improve power quality performance and ensure fast charging of the battery-supercapacitor system, voltage enhancement, enhancement of the power factor of the AC buses, in addition to the harmonic distortion reduction. The Whale Optimization Algorithm was proposed to optimize the gain values of the PID controller. The proposed controller ensures effective redundant fast charging as well as low decoupling of AC and DC sides with lower ripple content, inrush currents, and transient recovery switching voltages. A comparative evaluation of the performance of the presented SFC with the traditional D-STATCOM was presented for different states of charge conditions to imitate the performance of the storage scheme during the fast charging scenarios. The efficacy of the presented SFC was evaluated by time-domain simulations in the MATLAB/Simulink platform.

Keywords: FACTS devices; Whale optimization algorithm; harmonic distortion; PID controller; switched filters; grid-to-vehicle.

I. INTRODUCTION

In new era, electric vehicle (EVs) has emerged to offer an operative technique for the lessening of fossil fuel feasting, global energy request, and global heating [1]. Accordingly, it is a auspicious result to practice the diverse types of green-plugged-in hybrid EVs, which can be invigorated from renewable energy-based power production that is called grid-to-vehicle (G2V), where the voltage is forced by the grid and the current of the EV battery charger. Also, it can feed a grid as a vehicle-to-grid (V2G) arrangement. These machineries have several evidences such as low noise levels, zero emission, fuel efficiency, and high efficiency in transportation schemes [2], [3].

[1] Electrical Power and Machines Engineering Department, The Higher Institute of Engineering at El-Shorouk City, Cairo, Egypt.

* Corresponding Author: a.omar@sha.edu.eg

However, the growing use of EVs has led to the development of new practices in battery charger schemes to feed the huge battery packs [4]. In most cases, these packs need to be frequently recharged due to the limited capacity; thus, much attention is required to design fast charging schemes for the frequent charging process [5], [6]. A set of assessment indices that realize the charging modes can be used. The choice of these indices depends on points of interest, such as capacity, thermal boundaries of the charger, and thermochemical boundaries of the storage system itself [7].

In addition, a supercapacitor can be coupled with batteries as a practical solution during short periods of time (absorbing energy during the regenerative braking or delivering energy in rapid transitions), frequent charging problems, and also to provide excessive energy required when the battery cannot do it [8]. In [9], the effects of the grouping of battery packs and supercapacitors have been presented for smoothing fast power fluctuations during charging and discharging of EV batteries of EVs.

In the literature, different classes and intelligent charging control schemes of energy storage elements were presented in many studies [10], [11]. A simple battery, a type of rechargeable lithium battery used in EVs, was developed and verified in [12], whereas focusing on efficient energy utilization of remote charging stations. A multi-control strategy used for interlinking converters of EVs' storage to enhance voltage levels in an island AC/DC microgrid was presented in [13]. Also, the intelligent control scheme for AC/DC converter was introduced in [14] to regulate the power factor (PF) of plug-in hybrid EVs.

Consequently, most electric vehicles (EVs) are now equipped with battery chargers incorporating active power filters (APFs) and Flexible AC Transmission Systems (FACTS)-based technologies, which play a crucial role in tackling power quality (PQ) issues [15]. Switched Filter Compensator (SFC) topologies have been increasingly adopted in EV applications to boost voltage permanency, suppress harmonics, reward for reactive power deficits, and provision energy sustainability. For instance, a novel technique to reduce ripple voltages and harmonic currents in battery chargers was presented in [16] using FACTS-based filter compensation patterns. Reference [17] introduced an efficient DC drive system for EVs powered by a hybrid lithium-ion battery–fuel cell green energy source, integrated with an SFC. Moreover, a new hybrid filter topology designed for photovoltaic systems used in vehicle-to-grid (V2G) applications was explored in [18], [19]. While these compensation topologies each offer distinct benefits and limitations, it is evident that an optimal design framework for such compensators has not yet been established or thoroughly investigated.

To address this gap, this study proposes an improved FACTS-based Switched Filter Compensator (SFC) for grid-to-vehicle (G2V) battery charging functions. The proposed system aims to improve power quality, decrease total harmonic distortion (THD), minimalize both AC and DC inrush currents, and enhance voltage stability. A dynamic control strategy is developed employing a three-level Weighted Modulated Proportional-Integral-Derivative (WM-PID) controller to govern the SFC. Additionally, the boost converter is regulated by a separate three-level PID control strategy to enable rapid charging of the energy storage procedure.

To optimize the PID controller gains, the Whale Optimization Algorithm (WOA based metaheuristic mimicking the hunting behavior of humpback whales—is employed. WOA offers fast convergence to global optima while effectively preventing local minima, meeting it well-suited for tuning complex control systems.

Furthermore, a comparative performance evaluation is conducted between the proposed SFC and a conventionally optimized Distribution Static Compensator (D-STATCOM) under identical operating conditions. The comparison focuses on key performance metrics, including the battery's State of Charge (SoC) as an indicator of storage system efficiency and THD levels. The effectiveness of the proposed SFC-based control policy is validated through offline simulations implemented in the MATLAB/Simulink environment.

II. SYSTEM UNDER STUDY

A. System arrangement

This work introduces an SFC type for ensuring sustainable energy efficiency, fast charging, and THD reduction in the buses/nodes of the G2V system, as illustrated in Fig. 1. The presented scheme utilizes an SPWM with two complementary (S_a and S_b) switches. One of these switches (S_a) is utilized with the SFC compensator to mitigate harmonics, improve PF, and enhance PQ performance. And the other one, S_b is employed to adapt the DC-link of the voltage and the line current. These switching signals are generated by WM-PID controls by means of bus voltage and current signals for adequacy of the storage structure. The complete stipulations of the system apparatuses are offered in the Appendix Section-Table A1. The next section discusses this control scheme in detail.

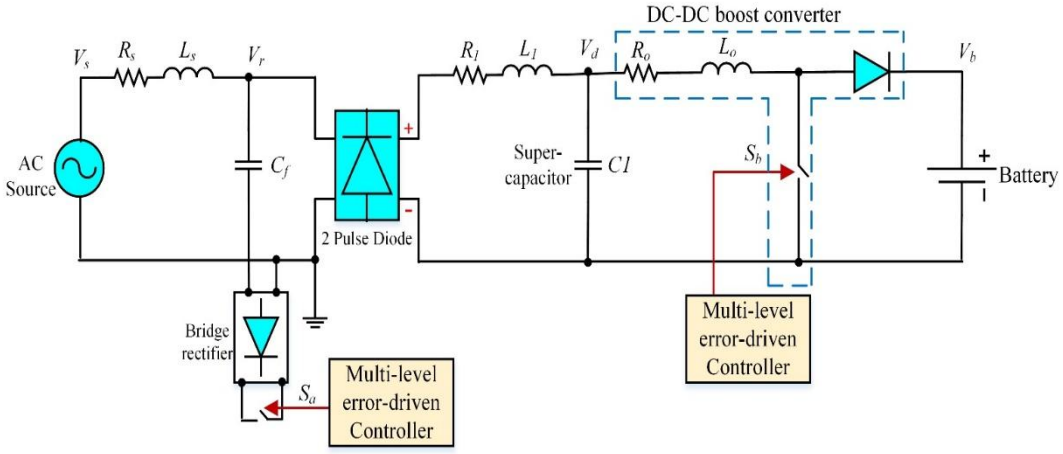

Figure 1. G2V modelling.

B. Lithium-ion battery

The most widely used battery type in this study is the Lithium-ion (Li-ion) battery, which has quickly become prevalent in high-performance electric vehicle (EV) applications [20], [21]. The electrical equivalent circuit (EEC) model employed as depicted in Fig. 2. The relationship governing this model is expressed by the following equation:

$$V_t = V_{oc} - I_L R_0 \quad (1)$$

The open-circuit voltage is strongly correlated with the battery's SOC, which ranges from 0% to 100%. The SOC is defined as shown in Eq. (2):

$$SOC = 100\left(1 - \frac{1}{Q}\int_0^t i_L(t)dt\right) \quad (2)$$

where Q represents maximum battery capacity (Ah).

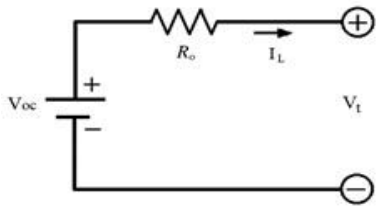

Figure 2. Li-ion battery modelling [22].

C. Supercapacitor

The supercapacitor (SC) model depicted in Fig. 3 was originally proposed by [25]. This model includes three key parameters: an equivalent series resistance (ESR), a parallel resistance

(R_p) and capacitance (C).

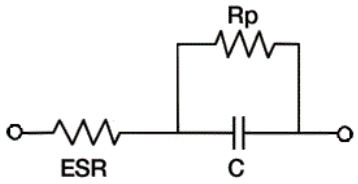

Figure 3. The equivalent circuit of the SC [26].

III. PRESENTED FILTER SCHEME

A. Boost converter

The most common topology of a boost DC/DC converter is illustrated in Fig. 4. The chopper consists of one electronic MOSFET switch that is the principle operation of the inverting topology for enhancing the flow of current and the output voltage at bus "*b*" on the DC side of the booster [28]. Contingent on the duty ratio (D), inductance voltage and current can be varied as follows:

1- If the switch is shut (S_{ON}), the current will be increased and flow in the series inductance, in addition to there is virtually no current passing in the storage system, which represents the coupling between the supercapacitor and battery.

2- When the switch is open (S_{off}), the current will be passed through DC filter L and diode to reduce the transient overvoltages and limit inrush currents. The output voltage can be calculated as:

$$V_o = \frac{V_{in}}{1-D} \tag{3}$$

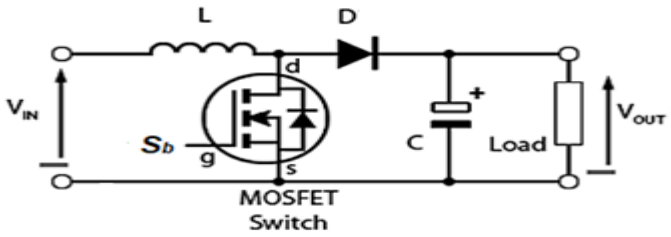

Figure 4. The boost converter circuit.

B. Multi-level regulation

The primary role of this three-level structure is to correct voltage and current errors on both the AC and DC buses associated with the 2-pulse diode rectifier. In this study, WM-PID controller is introduced (see Figs. 5(a)–5(c)). This controller generates two error signals, and , which originate from the three-level regulators and are used to drive a WM-PWM modulator. The WM-PWM, in turn, governs the timing sequences for injecting pulsating control signals into the MOSFET/IGBT switches. Specifically, switch actuates the proposed Solid-State Fuel Cell (SFC), while switch controls the boost converter.

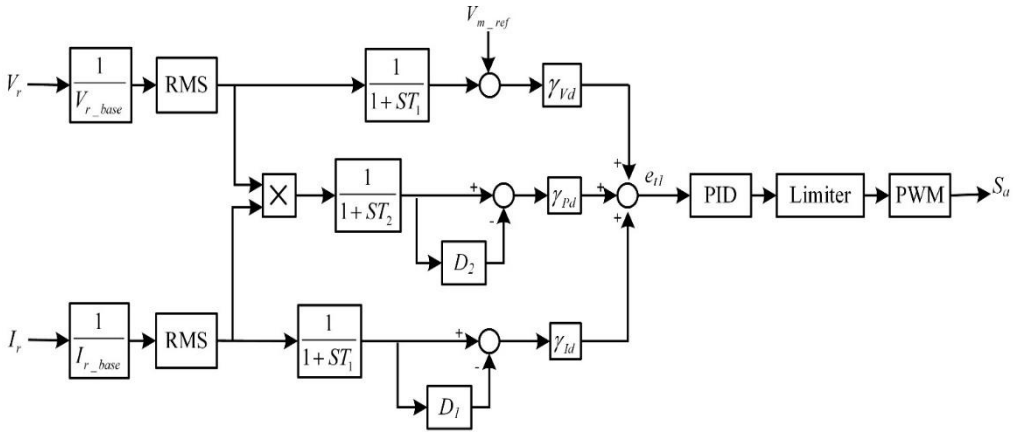

(a)

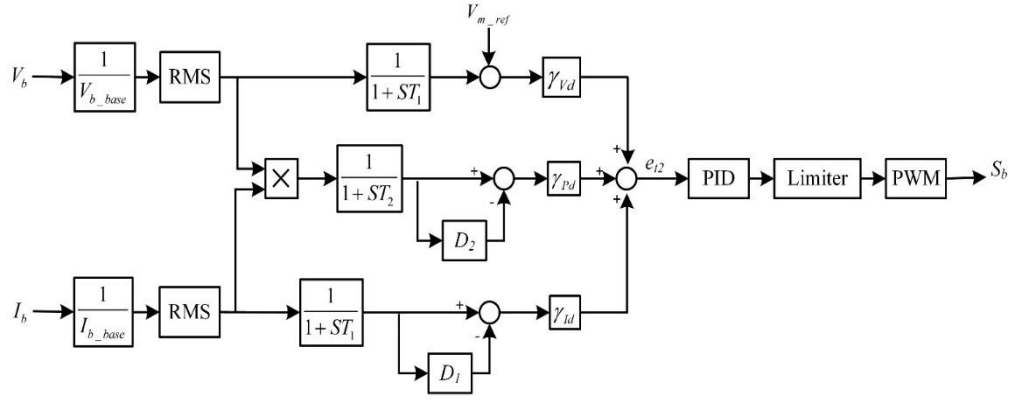

(b)

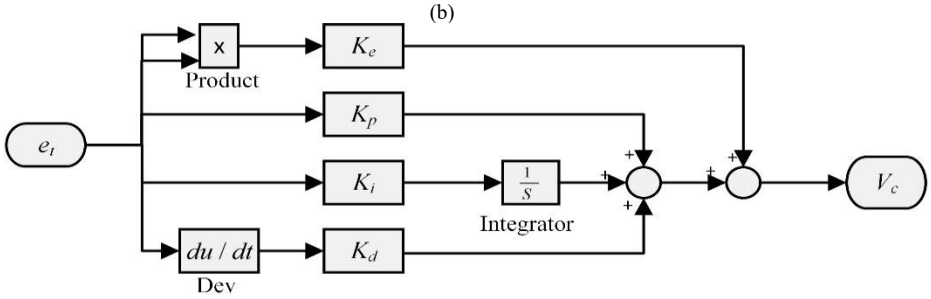

(c)

Figure 5. The planned controller: (a) PID of SFC, (b) PID of DC bus, (c) WM-PID controller.

The regulator responsible for controlling switch of the proposed SFC receives as inputs the voltage and current signals from the bus. The corresponding error signals for voltage, current, and power are defined as:

$$e_{Vr} = \frac{V_{mref} - V_r(\frac{1}{1+ST_1})}{Vr_{-base}} \quad (4)$$

$$e_{Ir} = \frac{I_r}{I_{r\ base}}(\frac{1}{1+ST_1})(1 - \frac{1}{1+ST_1}) \quad (5)$$

$$e_{Pr} = (\frac{V_r}{V_{m\_base}} x \frac{I_r}{I_{m\_base}})(1 - \frac{1}{1+ST_2}) \quad (6)$$

Similarly, the three-level regulator governing switch of the boost converter uses the voltage and current signals from the bus as inputs. Its associated error signals are specified by:

$$e_{Vb} = \frac{V_{mref} - V_b(\frac{1}{1+ST_1})}{Vb_{\_base}} \quad (7)$$

$$e_{Ib} = \frac{I_b}{I_{b\_base}}(\frac{1}{1+ST_1})(1 - \frac{1}{1+ST_1}) \quad (8)$$

$$e_{Pb} = (\frac{V_b}{V_{b\ base}} x \frac{I_b}{I_{b\ base}})(1 - \frac{1}{1+ST_2}) \quad (9)$$

The total error signals and are obtained by combining the individual voltage, current, and power errors through weighted summation, representing the integrated control objectives for the SFC and the boost converter, respectively. These are expressed in Eqs. (10) and (11):

$$e_{t1} = \gamma_{Vr}\,(e_{Vr}) + \gamma_{Ir}\,(e_{Ir}) + \gamma_{Pr}\,(e_{Pr}) \quad (10)$$

$$e_{t2} = \gamma_{Vb}\,(e_{Vb}) + \gamma_{Ib}\,(e_{Ib}) + \gamma_{Pb}\,(e_{Pb}) \quad (11)$$

Finally, in the time domain, the control signals and —which serve as the PWM command inputs for the SFC and the boost converter, respectively—are generated by the PID-based WM-PID controllers as follows:

$$V_{c1}(t) = K_{p1}\,(e_{t1}(t))^2 + K_{p1}\,e_{t1}(t) + K_{i1}\int_0^1 e_{t1}(t)dt + K_{d1}\frac{d(e_{t1}(t))}{dt} \quad (12)$$

$$V_{c2}(t) = K_{p2}\,(e_{t2}(t))^2 + K_{p2}\,e_{t2}(t) + K_{i2}\int_0^1 e_{t2}(t)dt + K_{d2}\frac{d(e_{t2}(t))}{dt} \quad (13)$$

III. FORMULATION OF THE OBJECTIVE FUNCTION

A. The fitness functions

To fine-tune the gains of the projected SFC-PID controller—namely (K_{p1}, K_{i1}, $K_{d1,}$ *and* K_{e1}) —which is integrated with the boost converter, as well as the gains of the D-STATCOM controller (K_{p3}, K_{i3}, $K_{d3,}$ *and* K_{e3}), also paired with the same booster, the following fitness function is demarcated:

$$\min(J_i) = \begin{Bmatrix} \min(J_1) = \min(0.5\int e_{t1}^2 + 0.5\int e_{t2}^2) \\ \min(J_2) = \min(0.5\int e_{t3}^2 + 0.5\int e_{t2}^2) \end{Bmatrix} \quad (15)$$

Here, J_i represents the total error for the *i*th controller configuration:

J_1 corresponds to the combined control system of the proposed SFC and the boost converter,

J_2 corresponds to the conventional D-STATCOM controller. This optimization is carried out subject to the following operational restrictions:

B. Limitations

The voltage level at the load bus must remain within permissible limits:

$$0.95 \le V_L \le 1.05 \quad (16)$$

The power factor at the load bus must be maintained as:

$$PF_{AC} \ge 0.9 \quad (17)$$

The THD of the voltage (THD_v) of the load bus, specified by:

$$\mathrm{THD_v} = \frac{\sqrt{\sum_{h=2}^{n} V_h^2}}{V_1} \quad (18)$$

$$\mathrm{THD_v} < \mathrm{THD_{v,max}} \quad (19)$$

The THD of the current (THD_i), given by (20), thus

$$\mathrm{THD_i} = \frac{\sqrt{\sum_{h=2}^{n} I_h^2}}{I_1} \quad (20)$$

$$\mathrm{THD_i} < \mathrm{THD_{i,max}} \quad (21)$$

C. Whale optimization algorithm (WOA)

Modeled after the intelligent bubble-net feeding behavior of humpback whales, the Whale Optimization Algorithm (WOA) is a swarm-based metaheuristic introduced by Mirjalili and Lewis in 2016 [29], [30]. The algorithm operates by having a population of search agents (whales) converge iteratively on the position of the best-found solution (the prey). To effectively navigate the search space, each agent chooses between two movement strategies: it can either encircle the prey in a contracting circle or follow

a spiral path towards it. This choice is governed by a probability parameter, ensuring a robust balance between exploring new areas (global search) and refining the solution in promising regions (local search).

$$\vec{X}(t+1) = \vec{X}_P(t) - \vec{A}.\vec{D} \quad (21)$$

$$\vec{D} = \left|\vec{C}.\vec{X}_P(t) - \vec{X}(t)\right| \quad (22)$$

Where $\vec{X}_P(t)$ denotes the position path of the best alternative at iteration t, and $\vec{X}(t)$ is the current location of a whale. The coefficient vectors $\vec{A}$ and $\vec{C}$ are defined as:

$$\vec{A} = 2\vec{a}.\vec{r} - \vec{a}; \qquad \vec{C} = 2.\vec{r} \quad (23)$$

$$\vec{a} = 2 - 2\frac{t}{t_{max}} \quad (24)$$

Here, $\vec{r}$ is a arbitrary vector in [0, 1], and $\vec{a}$ is a linearly declining vector that shrinks from 2 to 0 over the course of iterations, as given by:

$$\vec{X}(t+1) = \overrightarrow{D'}.e^{bl}.cos(2\pi l) + \vec{X}_P(t) \quad (25)$$

where $\overrightarrow{D'} = \left|\vec{X}_P(t) - \vec{X}(t)\right|$ represents the distance between the whale and the prey, b is a constant defining the shape of the logarithmic curve, and l is a arbitrary number uniformly distributed in [−1,1].

The algorithm employs a probability parameter to decide between the two movement strategies: if ρ<0.5, the reduction surrounding process is used; otherwise (ρ≥0.5), the spiral movement is applied. This probabilistic switching augments the algorithm's ability to perform both local exploitation and global exploration effectively.

A flowchart illustrating the WOA procedure is provided in Fig. 7. For further details on the Whale Optimization Algorithm, readers are referred to [31].

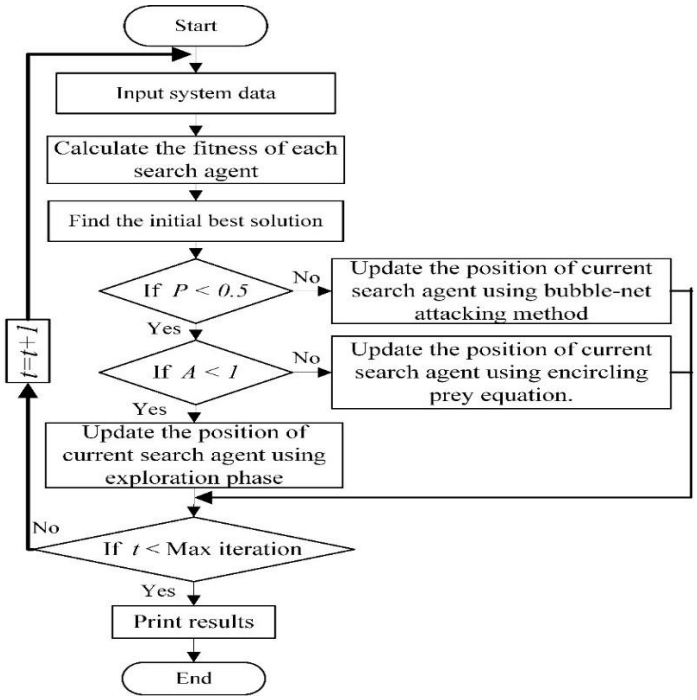

Fig. 7. Flowchart of whale optimization algorithm.

IV. SIMULATION RESULTS

Figures 8-13 show the various PQ indicators with D-STATCOM and with the proposed SFC under the change of SOC. The *SOC* is considered at 50% and full charging levels. The findings have been clarified in the split up at the buses "*s*" and "*r*".

A. Battery charging status (50%)

As illustrated in Figures 8 and 9, during half of the battery charging status, the proposed SFC scheme has a positive inspire on developing the PQ of the system. While using the proposed SFC, the current at

the bus ‘s’ is increased and reactive power has been declined. It can also be noted that the voltage is efficiently approaching 1 pu at the bus ‘r’.

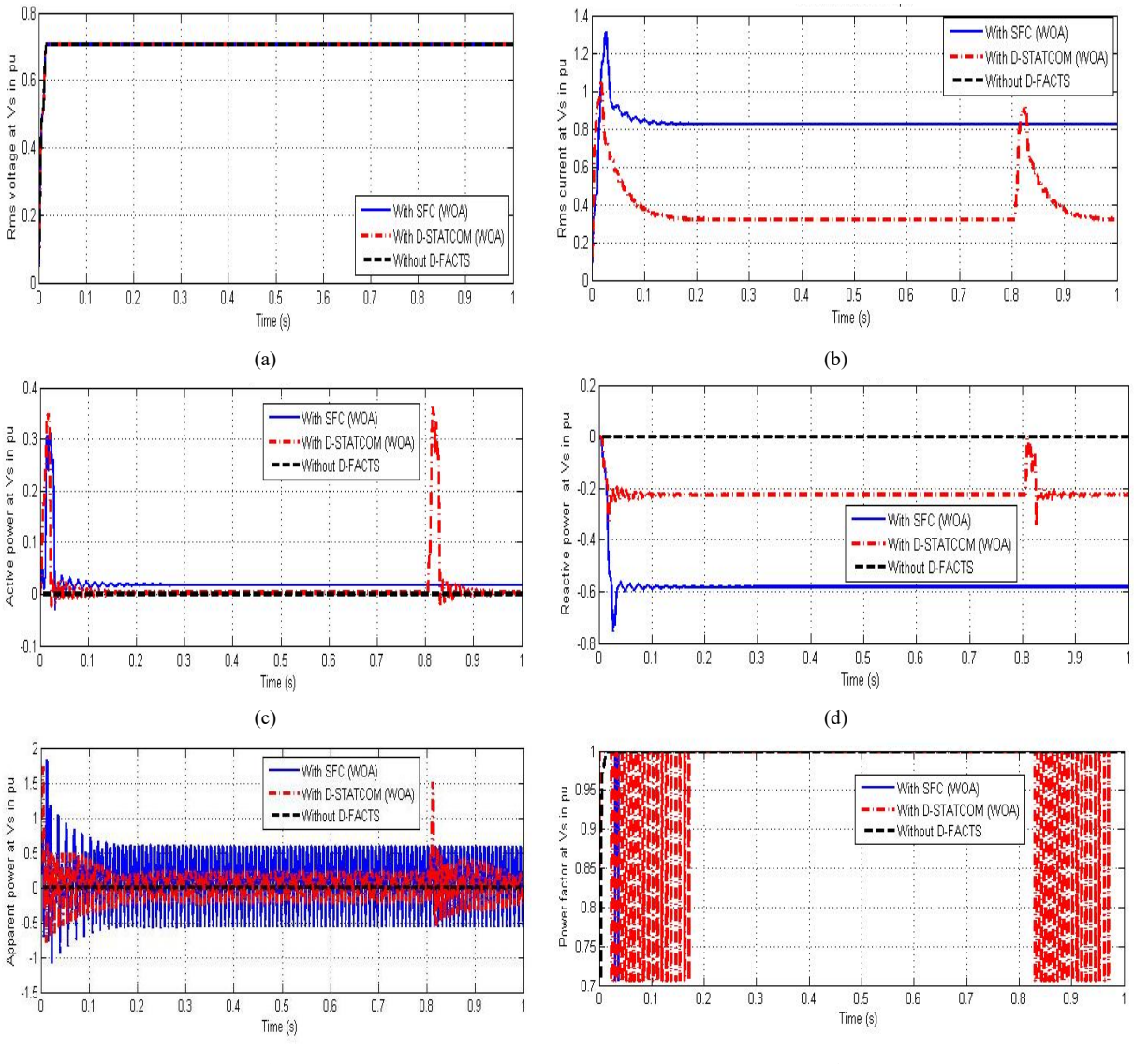

Figure 8. Simulated results at the V_s bus before and after compensation under 50% SOC using D-STATCOM: (a) V_{rms}, (b) I_{rms}, (c) P, (d) Q, (e) S, and (f) PF.

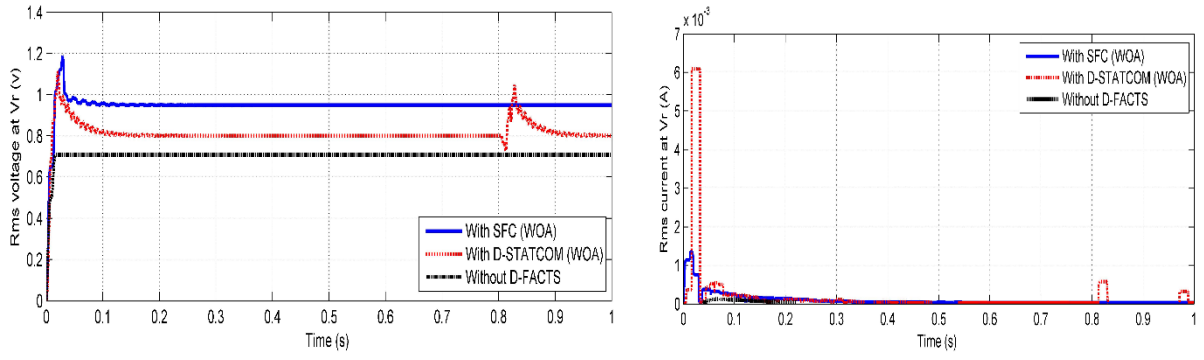

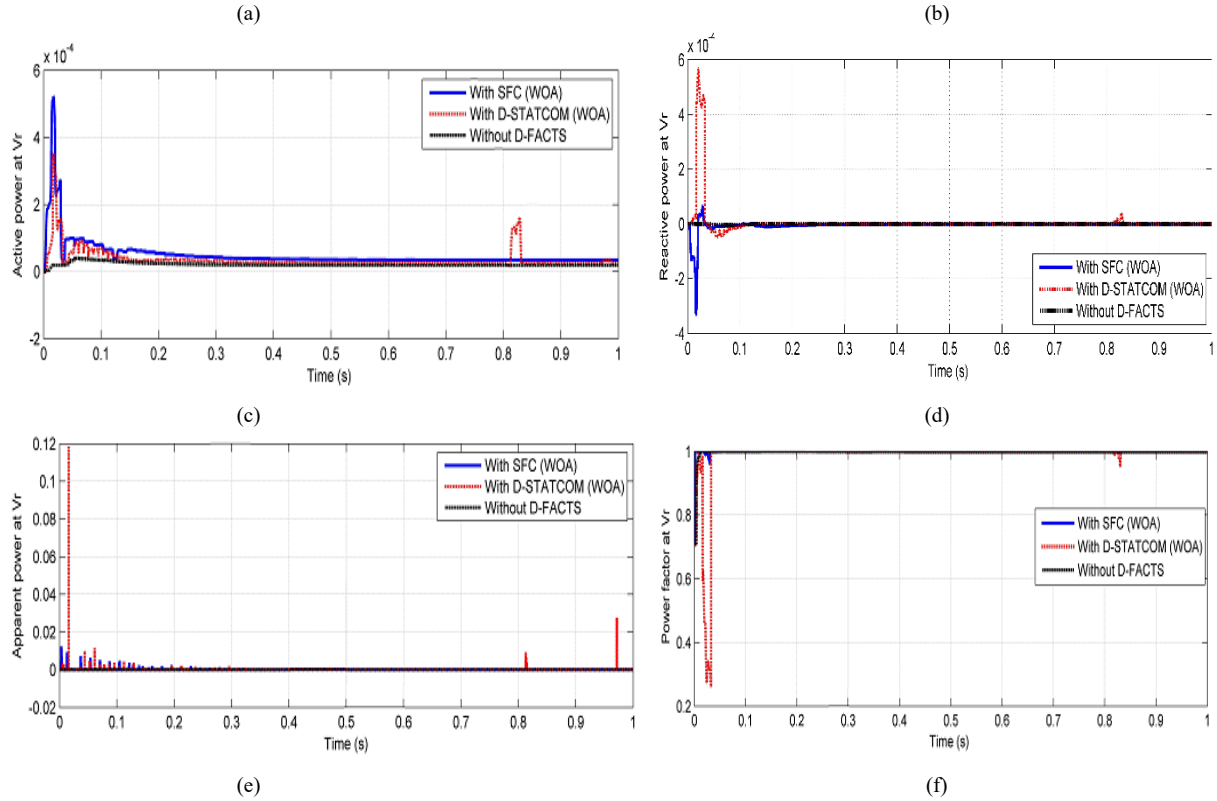

Figure 9. Simulated results at the V_s bus before and after compensation under 50% SOC using SFC: (a) V_{rms}, (b) I_{rms}, (c) P, (d) Q, (e) S, and (f) PF.

The value of PID controllers' parameters for SFC and D-STATCOM, in addition to the boost converter for both, is illustrated in Table I under 50% SOC.

TABLE I. PID CONTROLLERS; GAINS FOR SFC AND D-STATCOM DURING BATTERY CHARGING STATUS (50%)

	SFC-PID with the booster		**D-STATCOM-PID with the booster**	
	SFC-PID (K_{p1}, K_{i1}, K_{d1}, K_{e1})	Booster-PID (K_{p2}, K_{i2}, K_{d2}, K_{e2})	D-STATCOM-PID (K_{p3}, K_{i3}, K_{d3}, K_{e3})	Booster-PID (K_{p2}, K_{i2}, K_{d2}, K_{e2})
K_p	96.4543	32.8188	32.9449	31.6793
K_i	23.1837	14.0138	9.9288	2.1538
K_d	7.5860	6.5021	0.2732	0
K_e	0.5831	5	0.9436	1.0548

B. Full battery charging status (100%)

It can be seen from Figs. 10 and 11 that the rate of the voltage at V_s and V_r, when D-STATCOM is used, decreased below 1 pu, while the voltage at the same node is close to 1 pu over battery charging variations when the proposed SFC has been utilized. Also, the reactive power compensation has been decreased. As a result that the proposed SFC under full charging status has a positive impact on improving the power quality indices.

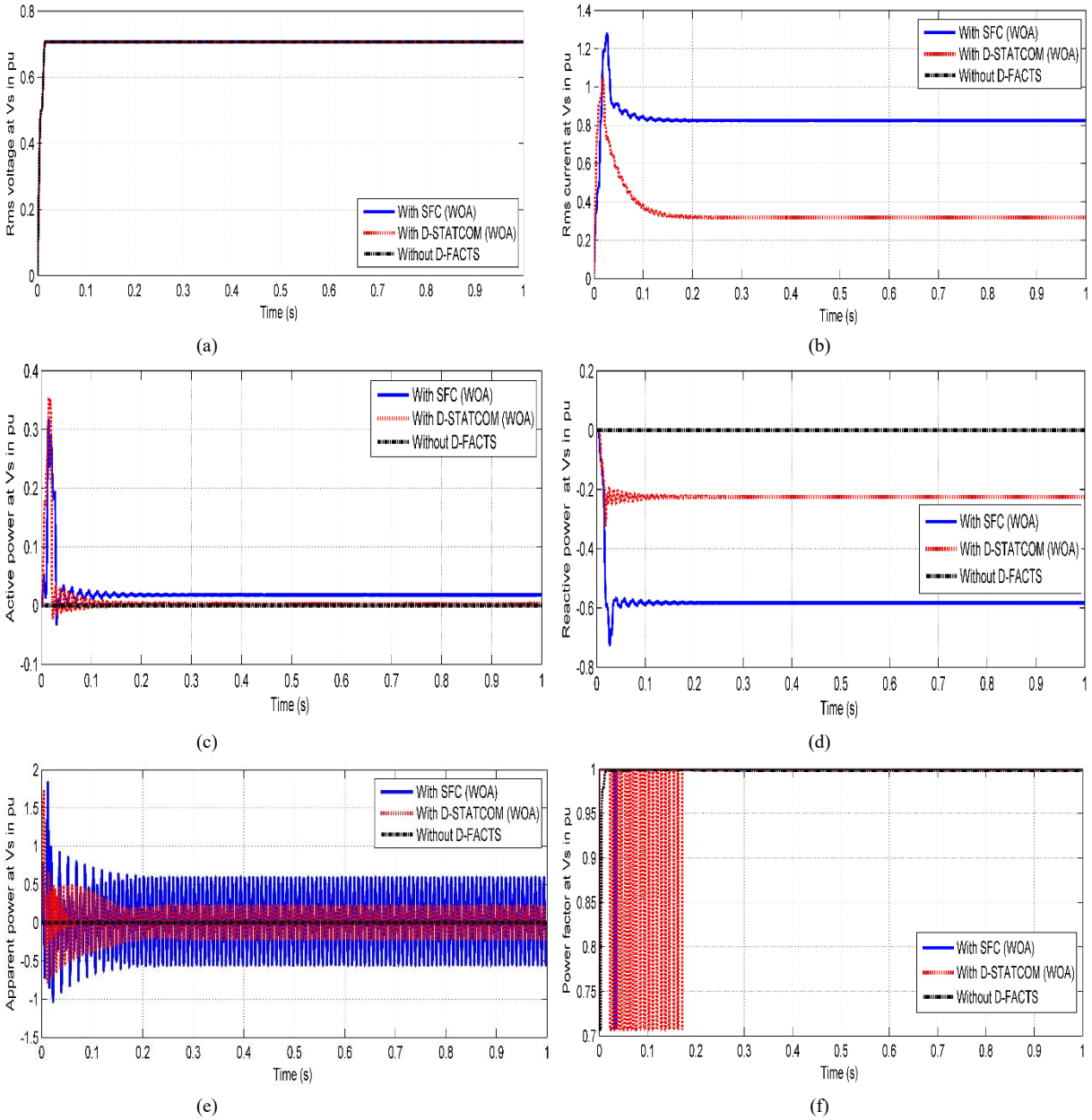

Figure 10. Simulated results (V_{rms}, I_{rms}, P, Q, S, PF) at the V_s bus before and after compensation under 100% SOC: (a) Rms voltage, (b) Rms current, (c) Active power, (d) Reactive power, (e) Apparent power, and (f) Power factor

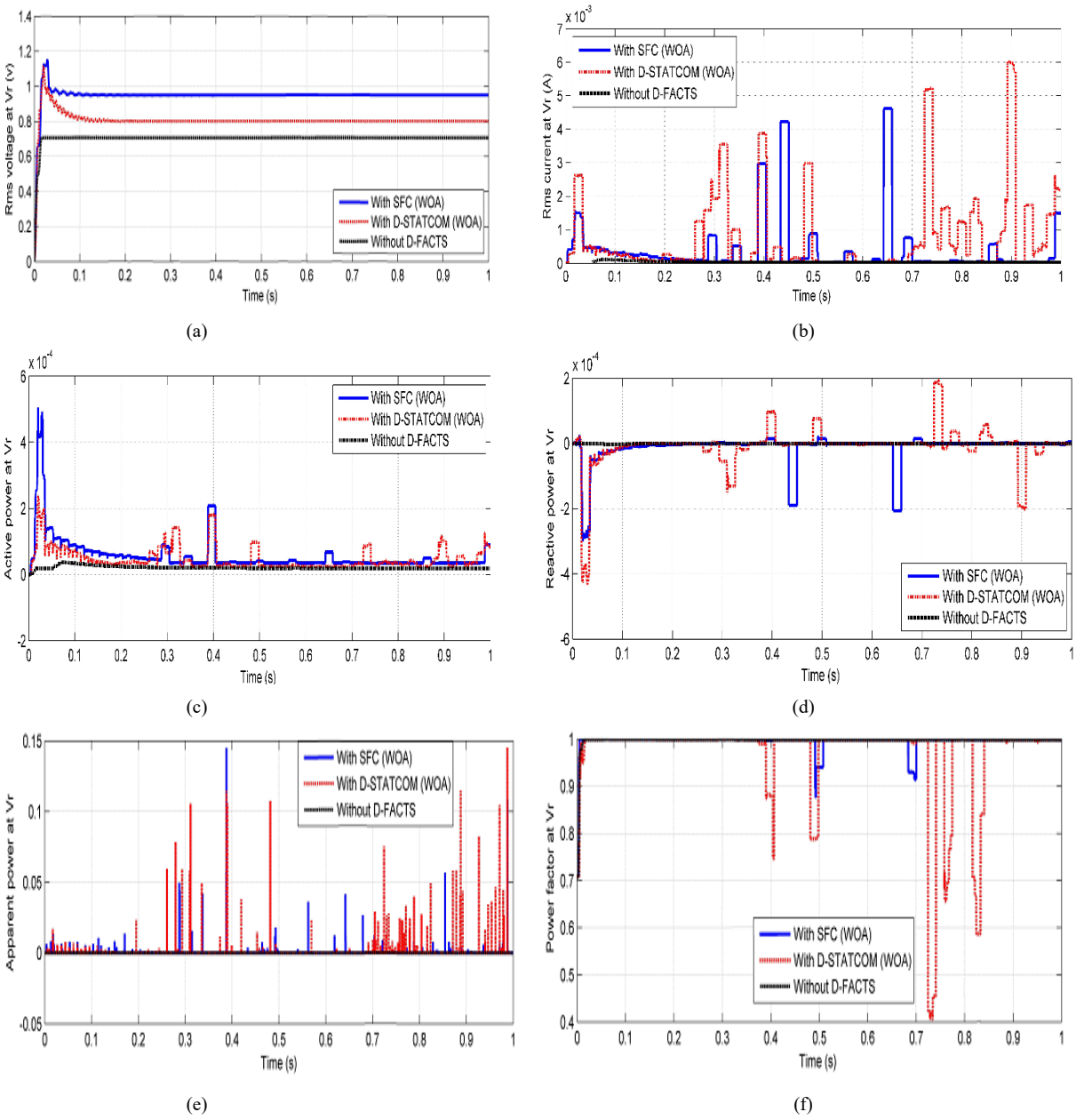

Figure 11. Simulated results at the V_s bus before and after compensation under 100% SOC: (a) V_{rms}, (b) I_{rms}, (c) P, (d) Q, (e) S, and (f) PF.

Table II presents the PID controller values for both the SFC and D-STATCOM, along with those for their respective boost converters, under 100% SOC.

TABLE II. PID CONTROLLERS FOR SFC AND D-STATCOM THROUGH 100% SOC.

	SFC-PID with the booster		**D-STATCOM-PID with the booster**	
	SFC-PID (K_{p1}, K_{i1}, K_{d1}, K_{e1})	Booster-PID (K_{p2}, K_{i2}, K_{d2}, K_{e2})	D-STATCOM-PID (K_{p3}, K_{i3}, K_{d3}, K_{e3})	Booster-PID (K_{p2}, K_{i2}, K_{d2}, K_{e2})
K_p	87.7338	113.8070	96.6277	77.9914
K_i	50	50	14.2740	0
K_d	5.9567	0	2.3908	0
K_e	3.8876	0	0.8730	2.3745

C. Analysis of harmonic distortions

Figure 12 presents the measured THD values for voltages and currents at the s and r buses before and after compensation. Further details on voltage and current harmonics, expressed in terms of THD, are summarized in Table III. The results clearly show that voltage harmonics have been substantially reduced—falling well within the permissible limits specified by IEEE standards [32], [33], [34]. Additionally, the THD of the current waveform at node s has also been notably decreased.

TABLE III. THD VALUES AT THE V_S AND V_R BUSES

THD	Without D-FACTS (%)	D-STATCOM (%)	SFC(%)
THD$_v$ at V_s bus	0.1	0.02	0.00
THD$_i$ at V_s bus	27.46	12.27	2.69
THD$_v$ at V_r bus	14.25	6.92	1.36
THD$_i$ at V_r bus	21.57	16.36	8.36

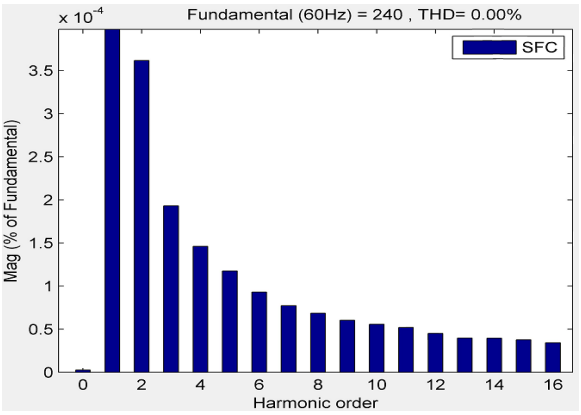

(a)

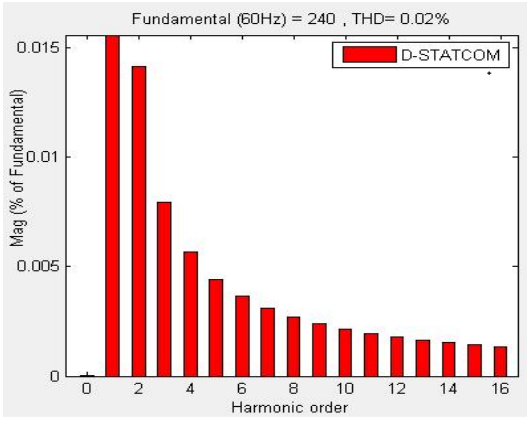

(b)

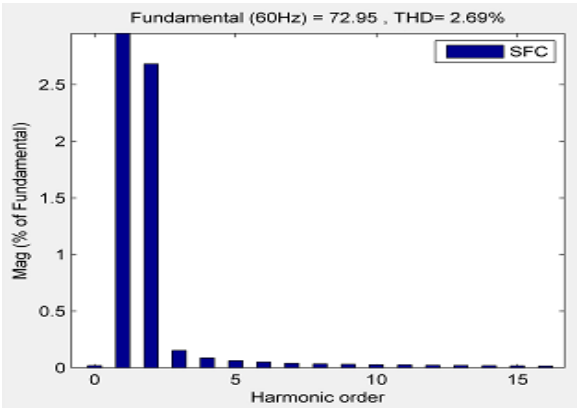

(c)

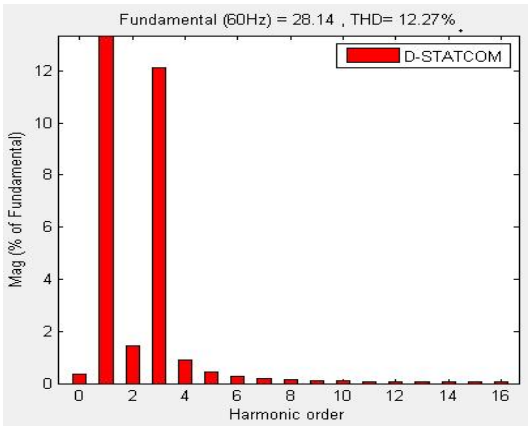

(d)

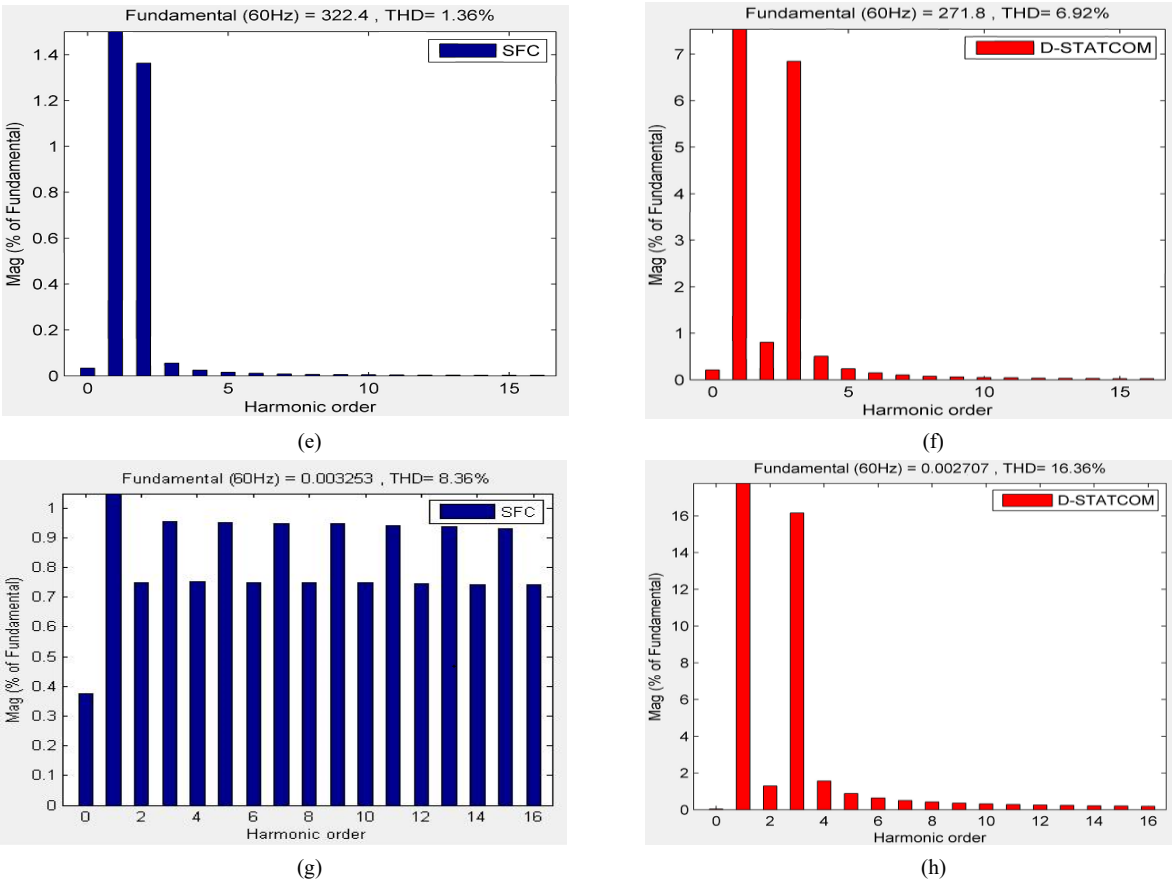

Figure 12. FFT of the voltages and currents at buses "s" and "r" (a) THD_v at bus "s" using SFC, (b) THD_v at bus "s" using D-STATCOM, (c) THD_i at bus "s" using SFC, (d) THD_i at bus "s" using D-STATCOM, (e) THD_v at bus "r" using SFC, (f) THD_v at bus "r" using D-STATCOM, (g) THD_i at bus "r" using SFC, (h) THD_i at bus "r" using D-STATCOM

V. CONCLUSION

The proposed robust switched filter compensator (SFC) combined with a Li-ion battery–supercapacitor hybrid storage arrangement and optimized using the Whale Optimization Algorithm (WOA) demonstrates significant improvements in power quality for grid-to-vehicle (G2V) battery charging applications. By employing a WM-PID control strategy, the system effectively enhances voltage stability, *reduces* total harmonic distortion (THD), minimizes inrush currents and ripple content, and improves power factor across varying states of charge. Comparative simulations against a traditional D-STATCOM under identical conditions confirm the superiority of the SFC scheme, particularly in maintaining bus voltages close to 1 pu and achieving THD levels well within IEEE standards during both partial (50%) and full (100%) battery charging scenarios. These results validate the efficacy, adaptability, and robustness of the proposed control and compensation architecture for next-generation fast-charging EV infrastructure.

APPENDIX

TABLE A1. THE COMPLETE DESCRIPTION OF THE SYSTEM COMPONENTS AND SUPERCAPACITOR

System specification		***Supercapacitor specification***	
System Part	***Values***	***System Part***	***Values***
AC source	230VAC, 50Hz	Rated voltage	300 V DC
Battery	300V DC, 4000 Ah	Rated capacitance	0.2 F
R_s	0.1 Ω	Equivalent DC series resistance	2.1 mΩ

L_s	3 mH	Surge voltage	305 V
Cf	550 µf	No. of series capacitance	4
$R_1 = R_0$	0.05 Ω	No. of parallel capacitance	1
$L_1 = L_0$	3 mH	Initial voltage	300 V

TABLE A2. THE COMPLETE DESCRIPTION OF SFC AND BOOST CONVERTER

SFC specification		***Boost converter specification***	
System Part	***Values***	***System Part***	***Values***
$V_{r\ base}$	230V	$V_{b\ ref}$	300V
$I_{r\ base}$	63A	$I_{b\ ref}$	60A
$V_{m\ ref}$	1 pu	$V_{m\ ref}$	1 pu
$\boldsymbol{\gamma_V = \gamma_I}$	1	$\gamma_V = \gamma_I$	1
$\boldsymbol{\gamma_P}$	0.6	γ_P	0.6
$T_1 = D_1$	10 ms	$T_1 = D_1$	10 ms
$T_2 = D_2$	20 ms	$T_2 = D_2$	30 ms
PWM frequency	3000 Hz	PWM frequency	4000 Hz

TABLE A3. THE COMPLETE DESCRIPTION OF D-STATCOM

System Part	***Specifications***
$V_{d\ base}$	180V
$I_{d\ base}$	37A
$I_{ss\ base}$	37A
$\boldsymbol{\gamma_{Vd} = \gamma_{Id}}$	1
$\boldsymbol{\gamma_{Pd}}$	0.5
$T_3 = D_3$	15 ms
$T_4 = D_4$	40 ms
PWM frequency	3000 Hz

REFERENCES

[1] A. M. Al-Ghaili, H. Kasim, H. Aris, and N. M. Al-Hada, "Can electric vehicles be an alternative for traditional fossil-fuel cars with the help of renewable energy sources towards energy sustainability achievement?," *Energy Informatics*, vol. 5, no. Suppl 4, p. 60, 2022, doi: 10.1186/s42162-022-00234-3.

[2] E. Mogire, P. Kilbourn, and R. Luke, "Electric Vehicles in Last-Mile Delivery: A Bibliometric Review," *World Electr. Veh. J.*, vol. 16, no. 1, p. 52, 2025, doi: 10.3390/wevj16010052.

[3] P. F. Borowski, "Economic and Technological Challenges in Zero-Emission Strategies for Energy Companies," *Energies*, vol. 18, no. 4, p. 898, 2025, doi: 10.3390/en18040898.

[4] A. Zentani, A. Almaktoof, and M. T. Kahn, "A Comprehensive Review of Developments in Electric Vehicles Fast Charging Technology," *Appl. Sci.*, vol. 14, no. 11, p. 4728, 2024, doi: 10.3390/app14114728.

[5] A. Mohammed, O. Saif, M. Abo-Adma, A. Fahmy, and R. Elazab, "Strategies and sustainability in fast charging station deployment for electric vehicles," *Sci. Rep.*, vol. 14, no. 1, 2024, doi: 10.1038/s41598-023-50825-7.

[6] D. Zhang *et al.*, "A multi-step fast charging-based battery capacity estimation framework of real-world electric vehicles," *Energy*, vol. 294, p. 130773, 2024.

[7] A. Aksoz, B. Asal, E. Biçer, S. Oyucu, M. Gençtürk, and S. Golestan, "Advancing Electric Vehicle Infrastructure: A Review and Exploration of Battery-Assisted DC Fast Charging Stations," *Energies*, vol. 17, no. 13, p. 3117, 2024.

[8] C. V. M. Gopi and R. Ramesh, "Review of battery-supercapacitor hybrid energy storage systems for electric vehicles," *Results Eng.*, vol. 24, p. 103598, 2024, doi: https://doi.org/10.1016/j.rineng.2024.103598.

[9] J. Zhang, M. Gu, and X. Chen, "Supercapacitors for renewable energy applications: A review,"

Micro Nano Eng., vol. 21, p. 100229, 2023, doi: https://doi.org/10.1016/j.mne.2023.100229.

[10] S. Wang *et al.*, "A comprehensive survey of the application of swarm intelligent optimization algorithm in photovoltaic energy storage systems," *Sci. Rep.*, vol. 14, no. 1, p. 17958, 2024.

[11] S. M. R. Rostami and Z. Al-Shibaany, "Intelligent energy management for full-active hybrid energy storage systems in electric vehicles using teaching–learning-based optimization in fuzzy logic algorithms," *IEEE Access*, vol. 12, pp. 67665–67680, 2024.

[12] J. Wang, J. Lv, W. Lin, W. Song, and Z. Feng, "Heat generation rate estimation of lithium-ion batteries for electric vehicles by BP-based optimized neural network," *Appl. Therm. Eng.*, vol. 253, p. 123752, 2024, doi: 10.1016/j.applthermaleng.2024.123752.

[13] A. Vora and R. Aparnathi, "Energy-Optimized Intelligent Distributed Energy Resources in a Microgrid," *Stat. Optim. Inf. Comput.*, 2025.

[14] E. Villa-Ávila, D. Ochoa-Correa, and P. Arévalo, "Advancements in Power Converter Technologies for Integrated Energy Storage Systems: Optimizing Renewable Energy Storage and Grid Integration," *Processes*, vol. 13, no. 6, p. 1819, 2025.

[15] S. R. Das *et al.*, "A review on different control strategies applied to power filter for power quality improvement," *Electr. Eng.*, pp. 1–29, 2025, doi: 10.1007/s00202-025-03153-0.

[16] D. Bhule and R. S. Kaarthik, "A Model Predictive Control Scheme for a Single-Phase Integrated Battery Charger With Active Power Decoupling for EV Application," *IEEE Trans. Power Electron.*, vol. 39, no. 4, pp. 4117–4126, 2024, doi: 10.1109/TPEL.2024.3350991.

[17] A. Benhammou, H. Tedjini, M. A. Hartani, R. M. Ghoniem, and A. Alahmer, "Accurate and Efficient Energy Management System of Fuel Cell/Battery/Supercapacitor/AC and DC Generators Hybrid Electric Vehicles," 2023. doi: 10.3390/su151310102.

[18] P. Hemachandu, S. Premalatha, K. P. Arunachalam, and P. V. H. Prasad, "Energy Management in Photovoltaic-Based Electric Vehicle Charging Systems With Battery Storage and Vehicle-to-Grid Support," *Energy Storage*, vol. 7, no. 5, p. e70236, 2025.

[19] E. Villa-Avila, P. Arevalo, D. Ochoa-Correa, V. Iniguez-Moran, and F. Jurado, "A New Adaptive Strategy for Enhancing the Stability of Isolated Grids through the Integration of Renewable Energy and V2G Management," *Appl. Sci.*, vol. 14, no. 14, p. 6380, 2024.

[20] S. Hemavathi, "India's Lithium-Ion Battery Landscape Strategic Opportunities, Market Dynamics, and Innovation Pathways," *Energy Storage*, vol. 7, no. 6, p. e70244, 2025.

[21] K. D. Rao, K. D. Rao, P. Pavani, K. V. S. R. Prasad, D. Indira, and B. Phaniteja, "A critical review on lithium ion battery modeling, battery management system and thermal runaway issues," *Electr. Eng.*, pp. 1–37, 2025.

[22] H. A. A. Ali, L. H. J. Raijmakers, K. Chayambuka, D. L. Danilov, P. H. L. Notten, and R. A. Eichel, "A comparison between physics-based Li-ion battery models," *Electrochim. Acta*, vol. 493, p. 144360, 2024, doi: 10.1016/j.electacta.2024.144360.

[23] C. Berna-Escriche, L. Álvarez-Piñeiro, and D. Blanco, "Optimization of Solar Generation and Battery Storage for Electric Vehicle Charging with Demand-Side Management Strategies," *World Electr. Veh. J.*, vol. 16, no. 6, p. 312, 2025, doi: 10.3390/wevj16060312.

[24] I. Arenas Kelbelova, "Study of a super capacitor solution as a replacement of an energy storing motor of 1500kW at OKG3 nuclear reactor," 2024.

[25] K. Dissanayake and D. Kularatna-Abeywardana, "A review of supercapacitors: Materials, technology, challenges, and renewable energy applications," *J. Energy Storage*, vol. 96, p. 112563, 2024, doi: 10.1016/j.est.2024.112563.

[26] A. He *et al.*, "Flexible Supercapacitor Integrated Systems," *Adv. Mater. Technol.*, vol. 9, no. 21, p. 2301931, 2024, doi: 10.1002/admt.202301931.

[27] A. Maulana, "Analysis of the Effect of Capacitor Installation and Rectifier Circuit on the Reciprocating Load of a Single-Phase AC Generator," *J. Mar. Electr. Electron. Technol.*, vol. 1, no. 1, pp. 1–8, 2023.

[28] E. Sangeetha and V. Ramachandran, "Different Topologies of Electrical Machines, Storage Systems, and Power Electronic Converters and Their Control for Battery Electric Vehicles—A Technical Review," *Energies*, vol. 15, no. 23, p. 8959, 2022, doi: 10.3390/en15238959.

[29] M. H. Nadimi-Shahraki, H. Zamani, Z. Asghari Varzaneh, and S. Mirjalili, "A systematic review of the whale optimization algorithm: theoretical foundation, improvements, and hybridizations," *Arch. Comput. Methods Eng.*, vol. 30, no. 7, pp. 4113–4159, 2023.

[30] S. Mirjalili and A. Lewis, "The Whale Optimization Algorithm," *Adv. Eng. Softw.*, vol. 95, pp. 51–67, 2016, doi: 10.1016/j.advengsoft.2016.01.008.

[31] N. Rana, M. S. A. Latiff, S. M. Abdulhamid, and H. Chiroma, "Whale optimization algorithm: a systematic review of contemporary applications, modifications and developments," *Neural Comput. Appl.*, vol. 32, no. 20, pp. 16245–16277, 2020.

[32] N. Cho, B. Wendha, and M. Luthfi, "Evaluations on the harmonic allocation methods of IEC 61000-3-6 and IEEE Standard 519 in the distribution systems," *Electr. Power Syst. Res.*, vol. 230, p. 110260, 2024.

[33] H. Chen, J. Wang, H. Hu, and Y. Huang, "Assessment of voltage harmonics' impact on the maximum load capacity of the power supply transformer for the LHCD system," *Sci. Rep.*, vol. 14, no. 1, p. 6332, 2024.

[34] N. Subramanian and A. A. Stonier, "A comprehensive review on selective harmonic elimination techniques and its permissible standards in electrical systems," *IEEE Access*, vol. 12, pp. 141966–141998, 2024.